Phase diagram of model anisotropic particles with octahedral symmetry

E. G. Noya and C. Vega
Departamento de Química-Física, Facultad de Ciencias Químicas, Universidad Complutense de Madrid, E-28040 Madrid, Spain

J. P. K. Doye
Physical and Theoretical Chemistry Laboratory, Oxford University, South Parks Road, Oxford, UK OX1 3QZ

A. A. Louis
Rudolf Peierls Centre for Theoretical Physics, 1 Keble Road, Oxford, UK OX1 3NP

(Dated: February 5, 2008)

We computed the phase diagram for a system of model anisotropic particles with six attractive patches in an octahedral arrangement. We chose to study this model for a relatively narrow value of the patch width where the lowest-energy configuration of the system is a simple cubic crystal. At this value of the patch width, there is no stable vapour-liquid phase separation, and there are three other crystalline phases in addition to the simple cubic crystal that is most stable at low pressure. Firstly, at moderate pressures, it is more favourable to form a body-centred cubic crystal, which can be viewed as two interpenetrating, and almost non-interacting, simple cubic lattices. Secondly, at high pressures and low temperatures, an orientationally ordered face-centred cubic structure becomes favourable. Finally, at high temperatures a face-centred cubic plastic crystal is the most stable solid phase.

I. INTRODUCTION

Anisotropic patchy particles consisting of a repulsive core with some attractive sites have been used to study a variety of problems. The first anistropic patchy potentials were introduced as models of associative liquids (see, for example, Refs. 1,2,3,4,5,6). More recently, anisotropic patchy models have received renewed interest in the context of protein crystallization.[7,8,9,10,11,12,13] Proteins are usually hard to crystallize, but, in order to determine the structure of a given protein, and hence its functionality, large crystals that can be used in high-resolution X-ray diffraction studies are needed.[14] In this respect, theoretical studies aiming to predict the conditions which favour crystallization would be very valuable. Even though some significant progress has already been made using simple isotropic potentials,[15,16] it is known that protein interactions are short-ranged and highly anisotropic. For example, most protein crystals have packing fractions that are much lower than the close-packed solids typically favoured by isotropic potentials.[17] So far, studies using anisotropic models have shown that the fluid-fluid coexistence moves to lower temperatures as the interactions become more anisotropic (either by decreasing the number of patches or making them smaller)[10] and can even become metastable.[7] The introduction of anisotropy can also induce the stability of multiple solid phases, including orientationally ordered and plastic phases.[11]

Anisotropic interactions have also received much attention in the context of the development of new materials. In particular, there has been increasing interest in the fabrication of colloids[18,19,20,21,22,23,24,25,26] and nanoparticles[27,28,29] with anisotropic interactions, one of the goals being to tailor their interactions so that they are able to self-assemble into a given target structure. One set of targets that has received particular attention is low-density colloidal crystals, e.g. colloidal diamond, because of their potential as photonic materials.[30] This work has stimulated a number of recent theoretical studies that have begun to address the question of how such patchy interactions can be used to control the crystallization behaviour[31,32] and the self-assembly of finite objects of given size and symmetry.[33,34,35,36] Some of the latter studies have also been motivated by a desire to understand biological self assembly, such as the formation of virus capsids.

The final area where anisotropic patchy models have been the subject of recent interest is in the study of the dynamics of supercooled liquids.[37,38,39,40] In particular, as patchy models tend to move the liquid-vapour coexistence line to lower temperature, and to lower packing fractions,[38] they make it much easier to study gels, i.e. dynamically-arrested states that have low density and where the arrest is due to formation of energetically stable bonds, rather than caging of the atoms in a densely-packed environment.

In spite of these studies, there is still much to be learnt from a fundamental point of view about how anisotropic interactions affect the thermodynamics and dynamics of a system. In particular, it is not fully understood how the arrangement of the patches will affect the phase diagram. It seems reasonable that if the patches are located at positions that favour the local environment of a given crystalline structure, crystallization into that structure would be favoured. On the other hand, a random distribution of the patches, as perhaps may be the case for the surface of a protein, will normally lead to a situation where the local order is not compatible with any crystalline lattice and, therefore, crystallization will be

hindered. However, relatively little is known about how the specificity of the angular interactions will affect the relative stability of the phases or their accessibility due to kinetic effects.

In this paper we study a model of patchy particles that we have previously used to study the self-assembly of monodisperse clusters,[36] and the kinetics of crystallization in two and three dimensions.[32] One of the intriguing results of the latter work was that crystallization of particles with six octahedrally-arranged patches into a simple cubic (sc) crystal appeared to be much easier than crystallization of particles with four tetrahedrally-arranged patches into a diamond lattice. Our hypothesis is that this difference in crystallization kinetics reflects the absence of frustration in the octahedral system, whereas in the tetrahedral system the preferred local order differs from the global crystalline order, thus frustrating crystallization. In order to understand this further a systematic study of the nucleation behaviour for these two systems is required, and a necessary precursor for such work is the computation of the phase diagram. This is one of the motivations for the present study, where we compute the phase diagram for particles with an octahedral arrangement of the patches. Furthermore, the phase diagram will also be of considerable interest in its own right, with the potential for competition between lower- and higher-density crystalline phases, and the possibility of plastic phases that have translational, but no orientational order.

II. METHOD

A. Model

Our model consists of spherical particles with a given number of attractive patches whose geometry is specified by a set of patch vectors. The total potential can be written as a sum of two-body terms that depend on the distance between two particles r_{ij}, but also on their relative orientations $\mathbf{\Omega}_i$ and $\mathbf{\Omega}_j$:

$$U(\mathbf{r}_1, ..., \mathbf{r}_n, \mathbf{\Omega}_1, ..., \mathbf{\Omega}_n) = \sum_{i=1}^{N-1} \sum_{j=i+1}^{N} V(r_{ij}, \mathbf{\Omega}_i, \mathbf{\Omega}_j) \quad (1)$$

The interaction between two particles is described by a potential with an isotropic repulsive core and an angular-dependent attractive term:

$$V(\mathbf{r}_{ij}, \mathbf{\Omega}_i, \mathbf{\Omega}_j) = \begin{cases} V_{LJ}(r_{ij}) & r_{ij} < \sigma_{LJ} \\ V_{LJ}(r_{ij}) V_{ang}(\widehat{\mathbf{r}}_{ij}, \mathbf{\Omega}_i, \mathbf{\Omega}_j) & r_{ij} \geq \sigma_{LJ} \end{cases} \quad (2)$$

where $V_{LJ}(r)$ is the Lennard-Jones potential:

$$V_{LJ}(r) = 4\epsilon \left[\left(\frac{\sigma_{LJ}}{r} \right)^{12} - \left(\frac{\sigma_{LJ}}{r} \right)^{6} \right] \quad (3)$$

ϵ is the pair well depth and $V_{LJ}(\sigma_{LJ}) = 0$. Additionally, for computational efficiency, the potential is truncated and shifted using a cutoff distance of $2.5\,\sigma_{LJ}$. The attractive interaction is modulated by a product of Gaussian functions that are centred at the position of each patch:

$$V_{ang}(\widehat{r}_{ij}, \mathbf{\Omega}_i, \mathbf{\Omega}_j) = \exp\left(-\frac{\theta^2_{k_{min},ij}}{2\sigma^2} \right) \exp\left(-\frac{\theta^2_{l_{min},ji}}{2\sigma^2} \right), \quad (4)$$

where σ is the standard deviation of the Gaussian, $\theta_{k,ij}$ ($\theta_{l,ji}$) is the angle formed between patch k (l) on atom i (j) and the interparticle vector $\mathbf{r}_{ij}$ ($\mathbf{r}_{ji}$), and k_{min} (l_{min}) is the patch that minimizes the magnitude of this angle. The interaction is a maximum when both patches are pointing at each other along the interparticle vector $\mathbf{r}_{ij}$ and it will decrease as the particles deviate further from this equilibrium orientation. A schematic representation of two such interacting particles is provided in Fig. 1.

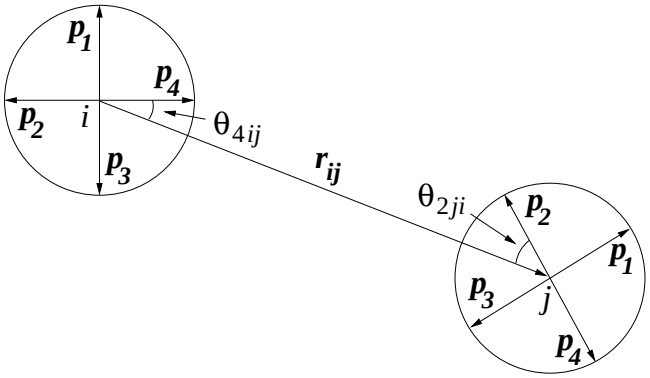

FIG. 1: A schematic representation of the geometry of the interaction between two particles. For clarity, we depict a two-dimensional analogue of the three-dimensional model used in this work. In this two-dimensional model, the particles have four patches arranged regularly with their directions described by the patch vectors, p_i. In the particular case shown in the figure, patch 4 on particle i interacts with patch 2 in particle j because they are the closest to the interparticle vector.

The angular dependence of Eq. 4 mimics the orientational dependence that exists in short range directional forces as is the case for hydrogen bonding. The use of $\theta_{k_{min},ij}$ and $\theta_{l_{min},ji}$ means that for a given pair of particles only a single patch on each particle is involved in the interaction, i.e. the possibility of 'double hydrogen bonding' is removed by the use of Eq. 4.

One of the advantages of this potential is its simplicity. It is easy to implement and it is computationally not very expensive to evaluate. Furthermore, the model includes the anisotropy in a very simple and flexible way. Simply by changing the number and position of patches, each of which is defined by a vector in the particle reference system, it is possible to obtain a wide range of anisotropic potentials. Another advantage is that the well-characterized Lennard-Jones potential can be obtained as a limiting case of the current model when the width of the patches becomes increasingly large. This feature can be particularly useful if one wants to study

the effect of the anisotropy, going from a very anisotropic model to the isotropic limit.

We shall use reduced units throughout, so that $U^* = U/\epsilon$, $p^* = p/(\epsilon/\sigma_{LJ}^3)$, $T^* = T/(\epsilon/k_B)$ and $\rho^* = \rho\sigma_{LJ}^3$. Consequently, the only parameter that needs to be specified to fully characterize the interaction between two particles is σ, i.e., the angular width of the attractive patches (see Eq. 4). In the present calculations, we use particles with six patches that have an octahedral arrangement, and since we wish to study the model in a regime where there is a stable low-density crystal, we have chosen to use a relatively narrow patch width, namely σ =0.3 radians. In previous work[32] it has been shown that, for this value of σ and at not very high pressures, a low density sc crystal is formed spontaneously from the liquid at sufficiently low temperature. In particular, at a constant pressure p^* =0.1 crystallization occurred at $T^* \approx$0.17.

B. Solid structures

There are several crystalline structures that one might expect to be stable for particles with an octahedral arrangement of the patches. The most simple structure is a simple cubic crystal. In this structure, each of the six patches points directly at one of the six nearest neighbours, and none of the interactions will be frustrated. However, this crystal has a relatively low density, e.g. if the nearest-neighbour separation is equal to the minimum in the pair potential, $\rho^* = 1/\sqrt{2} = 0.707$, and so it is expected that new denser crystalline phases will appear when the system is exposed to moderate to high pressures.

Two possible higher-density crystals are the body-centred-cubic (bcc) and face-centred-cubic (fcc) lattices. However, in these structures, due to the symmetry of the potential, it is not possible to orient the particles so that each patch is pointing directly towards one of its nearest neighbours. For a bcc crystal, it is possible to simultaneously align only two of a particle's patches with its first neighbours. However, an orientationally ordered structure can be formed when the six patches of a given particle are pointing towards its six second nearest neighbours (see Figure 2). This structure can also be viewed as two interpenetrating simple cubic lattices that, as we will show, almost do not interact with each other. As the patches form an angle of $\pi/4$ radians with the first neighbours, there will almost be no interactions between first neighbours, except when they are closer than the repulsive barrier (σ_{LJ}). Furthermore, when the nearest-neighbours separation is σ_{LJ}, the distance betweeen second nearest neighbours is $2\sigma_{LJ}/\sqrt{3} = 1.1547\sigma_{LJ}$ which is only slightly longer than the minimum in the pair potential that occurs at $2^{1/6}\sigma_{LJ} = 1.1225\sigma_{LJ}$. Therefore, the energetic cost of interpenetrating the two lattices is relatively small, but as the density is significantly higher ($\rho^* = 1.299$ for the above geometry) the bcc lattice will have a more favourable enthalpy at moderate pressures.

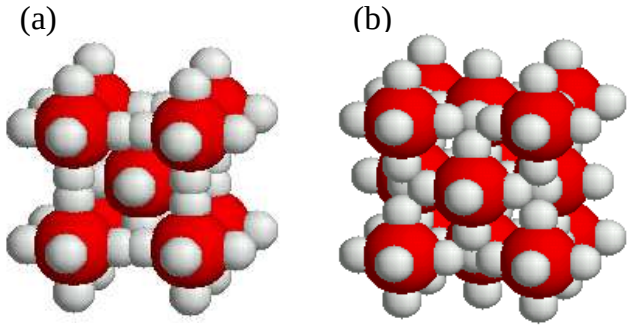

FIG. 2: (Colour online) Unit cells of the (a) bcc and (b) orientationally ordered fcc-o structures. As mentioned in the text, in both cases the patches are aligned with the second neighbours.

In some senses, this structure has similarities to the structures of ice VII and ice VIII. Both consist of two interpenetrating cubic ice lattices that do no have any interconnecting hydrogen bonds between them.[41]

For the fcc lattice, it is also possible to generate an orientationally-ordered structure, where the six patches are pointing towards six of the second nearest neighbours (we refer to this structure, which is depicted in Figure 2, as fcc-o). However, it is significantly higher in energy than the bcc lattice, because in this case the ratio of the second to the first nearest-neighbour distance is $\sqrt{2}$, and so if there is to be no repulsion between nearest neighbours (e.g. if their separation is σ_{LJ} and $\rho^* = \sqrt{2}$) then the second nearest neighbours are significantly further apart than the minimum in the pair potential.

It is also possible to generate an orientationally-ordered tetragonal crystal, in which the centres of mass of the particles are disposed as in a fcc lattice, but where four of the patches point towards first neighbours and the other two patches point towards second neighbours. This structure has a body-centred tetragonal unit cell ($a = b \neq c$, where a, b and c are the moduli of the lattice vectors), as the cubic symmetry of the fcc lattice has been broken due to the orientation of the particles (see Figure 1 in Reference 42 for an explanation of how to get the tetragonal unit cell in an analogous structure for a model of oppositely charged colloids). However, in NpT simulations in which each of the edges of the box was allowed to vary independently, we found the tetragonal crystal to undergo a transformation to an orientationally ordered bcc lattice. This type of deformation has been previously observed in other systems, and it is an example of a martensitic transition.[42] The transformation occurs by a shortening of the c edge, until $c = a$ and cubic symmetry is recovered. In view of these results, we have not further considered the tetragonal structure in our calculations. Nevertheless, one cannot exclude the possibility that there might be some range of pressure and temperature where the tetragonal structure is thermodynamically stable.

At sufficiently high temperatures when the attractive interactions become negligible, a translational ordered, but orientationally disordered fcc structure, i.e. a plastic phase, will also appear. We refer to this structure as fcc-d (or PC).

C. Equation of state for the fluid and solid phases

The equation of state for the solid and the liquid phases was calculated using Monte Carlo (MC) simulations in the NpT ensemble. Between 10 and 20 simulations were performed to determine the equation of state along each isotherm. Each simulation consisted of 40000 MC cycles, following an equilibration period of the same length. A MC cycle was defined as N attempts to translate a particle, plus N attempts to rotate a particle and two attempts to change the volume of the simulation box, N being the number of particles in the system. During the equilibration period, the maximum translational and rotational displacements were adjusted to obtain a 40% acceptance probability and the maximum volume change was chosen to obtain a 30% acceptance probability. In all the simulations, the output configuration of a given state was used as the input for the following simulation. The number of particles used in our calculations was 216 for the sc phase, 250 for the bcc phase, 256 for the fcc-o and fcc-d phases and 250 for the fluid phase. In all the cases, the length of the box was larger than twice the cutoff in the potential. Since all the solid structures that we considered were cubic, we performed NpT simulations with isotropic scaling.

D. Free energy calculations

At at given temperature, coexistence between two phases occurs at the pressure p where the chemical potential μ is the same for both phases. Since $\mu/k_BT = G/Nk_BT = A/Nk_BT + pV/Nk_BT$ and the compressibility $z = pV/Nk_BT$ can be obtained via NpT simulations, a procedure to determine the Helmholtz free energy is needed.

The free energy of the fluid phase was estimated by integration from a very low density state, where the fluid can be considered to behave as an ideal gas:

$$\frac{A(\rho)}{Nk_BT} = \frac{A^{id}(\rho)}{Nk_BT} + \int_0^\rho \frac{z(\rho')-1}{\rho'} d\rho' \tag{5}$$

where $A^{id}(\rho)/Nk_BT = \ln(\rho\Lambda^3) - 1$. We took $\Lambda = \sigma_{LJ}$ because its value does not affect the coexistence properties.

For the solid phases, we used the method described by Frenkel and Ladd[43,44], as extended to non-spherical potentials.[4,45,46,47,48] In this method, the free energy is obtained by integration from the interacting Einstein crystal, whose interactions are described by the Hamiltonian:

$$\begin{aligned}\frac{H(\lambda_1^*,\lambda_2^*)}{k_BT} = \frac{H_0}{k_BT} + \lambda_1^* \sum_{i=1}^{N} \left(\sin(\Psi_a)^2 + \sin(\Psi_b)^2\right) \\ + \lambda_2^* \sum_{i=1}^{N} (\mathbf{r}_i - \mathbf{r}_{0,i})^2\end{aligned} \tag{6}$$

On the right hand side of this equation, H_0 is the original potential and the second and third terms are, respectively, an orientational and a translational field that tend to keep the particles at the positions and orientations of the perfect orientationally ordered lattice. In the term for the orientational field, Ψ_a is the minimum angle formed by any of the vectors that define the position of the patches in the particle's reference system with respect to the x axis of a fixed reference system and Ψ_b is the analogous quantity with respect to the y axis, where the fixed reference system has been chosen to be coincident with the orientation of the patches in the perfect lattice. As the patch that defines both angles must not be the same, when the same patch yields the minimum angle with both the x and y axes, the patches that form the second least angles were also computed. The patches that will contribute to the orientational field will be the pair that leads to the lowest energy for this term. Note that the orientational field has been chosen so that it has the same symmetry as the particles.

In the term for the translational field, $\mathbf{r}_{0,i}$ is the lattice position of particle i (as given by its centre of mass). $\lambda_1^* = \lambda_1/k_BT$ and $\lambda_2^* = \lambda_2/(k_BT\sigma_{LJ}^2)$ are the coupling parameters of the translational and orientational field, respectively. For practical reasons, we chose to use $\lambda_1^* = \lambda_2^* = \lambda^*$, i.e. both fields are switched on simultaneously. With this choice, the integral to the reference translational and orientational Einstein crystals can be performed at the same time, thus reducing the number of simulations needed to perform the numerical integration to the reference system. However, other choices of λ_1 and λ_2 are equally valid. Therefore, by using the same coupling parameter for both fields, Eq. 6 can be simplified into the following form:

$$\begin{aligned}\frac{H(\lambda^*)}{k_BT} = \frac{H_0}{k_BT} + \lambda^* \sum_{i=1}^{N} \left(\sin(\Psi_a)^2 + \sin(\Psi_b)^2\right) \\ + \lambda^* \sum_{i=1}^{N} (\mathbf{r}_i - \mathbf{r}_{0,i})^2\end{aligned} \tag{7}$$

The free energy difference between our model and the reference Einstein crystal (ΔA_2) is given by:

$$\frac{\Delta A_2}{Nk_BT} = \int_{\lambda^*_{max}}^{0} \left\langle \frac{\partial(H(\lambda^*)/Nk_BT)}{\partial\lambda^*} \right\rangle_{\lambda^*} d\lambda^* \tag{8}$$

This integral was evaluated numerically using a Gauss-Legendre quadrature formula, with 10 or 20 points depending on the case (a larger number of points is needed for the orientationally disordered plastic phase).

The free energy of a non-interacting Einstein crystal is already known,[43] and the free energy difference between an interacting and a non-interacting crystal (ΔA_1) can be calculated numerically by averaging the interparticle energy over a simulation of the non-interacting Einstein crystal:[43,49]

$$\frac{\Delta A_1}{Nk_BT} = \frac{U_0}{Nk_BT} - \frac{1}{N}\ln\left\langle \exp\left[-\left(\sum_{i=1}^{N-1}\sum_{j=i+1}^{N}\frac{V(r_{ij},\Omega_i,\Omega_j)}{k_BT} - \frac{U_0}{k_BT}\right)\right]\right\rangle, \quad (9)$$

where U_0 is energy of the perfect lattice. The maximum value of λ^* in Eq. 8 was chosen so that the structure of the interacting Einstein crystal defined by Eq. 6 was very similar to the perfect orientationally ordered lattice.

The free energy of the orientational field can be estimated numerically by integrating its partition function over all the orientations:[4,11]

$$\frac{A^{orient}}{Nk_BT} = -\ln\left(\tfrac{1}{8\pi^2}\int \exp\left\{-\lambda^*\left[\sin(\Psi_a)^2+\sin(\Psi_b)^2\right]\right\}\times \sin(\alpha)d\alpha d\phi d\gamma\right) \quad (10)$$

where Ψ_a and Ψ_b depend on the three Euler angles, α, ϕ and γ. This integral was evaluated numerically using the Monte Carlo integration method and using at least 10^9 points.

The final expression for the free energy of the solid is:

$$A^{tot} = A^{Einstein} + \Delta A_1 + \Delta A_2 + \Delta A_3 \quad (11)$$

where $A^{Einstein}$ is the sum of the free energy of the translational Einstein crystal[43] plus the free energy of the orientational field A^{orient}. The term ΔA_3 accounts for the fact that the integration to the Einstein crystal was evaluated by performing simulations in which the centre of mass of the system was fixed (see Ref. 43).

Once the free energy is known for a given state, the free energy along an isotherm can be obtained by integrating the equation of state:

$$\frac{A(\rho_2)}{Nk_BT} = \frac{A(\rho_1)}{Nk_BT} + \frac{1}{k_BT}\int_{\rho_1}^{\rho_2}\frac{p(\rho)}{\rho^2}d\rho \quad (12)$$

The coexistence points are determined by imposing the conditions of equal pressure and chemical potential, and can be obtained by plotting the chemical potential against the pressure for both phases. Coexistence is where the curves for the two phases cross, and Fig. 3 shows such a plot for the bcc and the fluid phases at $T^* = 0.243$.

E. Coexistence lines

The coexistence lines have been located using the Gibbs-Duhem integration method introduced by Kofke.[50,51] In this method the coexistence line is obtained by integration of the Clausius-Clapeyron equation:

$$\left(\frac{dp}{dT}\right) = \left(\frac{\Delta u + p\Delta v}{T\Delta v}\right) \quad (13)$$

where Δu and Δv are the molar energy change and molar volume change, respectively, between the two coexisting phases.

The Clausius-Clapeyron differential equation was solved numerically with a fourth order Runge-Kutta algorithm, and using as the initial conditions the coexistence points obtained with the thermodynamic integration method. The value of the integrand in each of the four steps of the Runge-Kutta method was evaluated by means of NpT simulations that consisted of 10000 MC cycles, following 10000 cycles of equilibration.

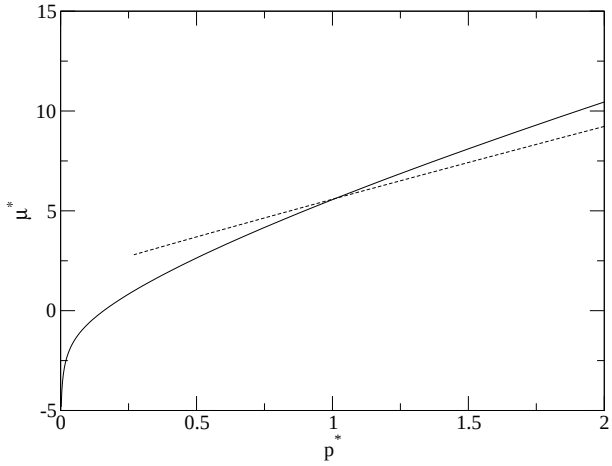

FIG. 3: Determination of the coexistence point between the fluid (solid line) and the bcc (dashed line) phases at $T^* = 0.243$.

F. Direct coexistence simulations

As a check of the above calculations, the melting points of the three solid phases were also estimated using the direct coexistence method, first proposed by Ladd and Woodcock.[52] In this work, we will follow the same procedure as the one described in Ref. 53. A crystal with around 400-500 particles was generated and subsequently equilibrated in the NpT-ensemble at a given pressure and temperature. This configuration was copied and heated to obtain a liquid configuration, which was then equilibrated at the same conditions as the solid but using a NpT-ensemble in which the volume of the simulation box can only change by modifying one of the box lengths, which we chose to be the box length along the z direction. Therefore, both the solid and liquid phases have the same periodic conditions along the x and y axes, and a solid-liquid interface can be built by simply joining the liquid and solid configurations along the $x-y$ plane.

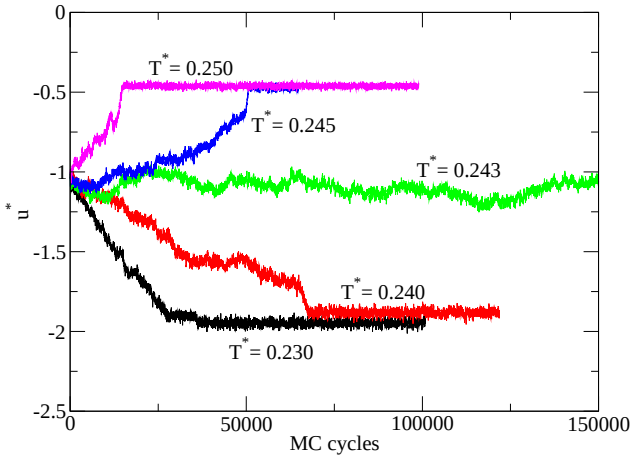

FIG. 4: (Colour online) The variation of the internal energy per particle ($u^* = U^*/N$) during NpT simulations of a box containing the bcc solid in contact with the fluid at $p^* = 1.0$. A few trajectories at different temperatures are shown.

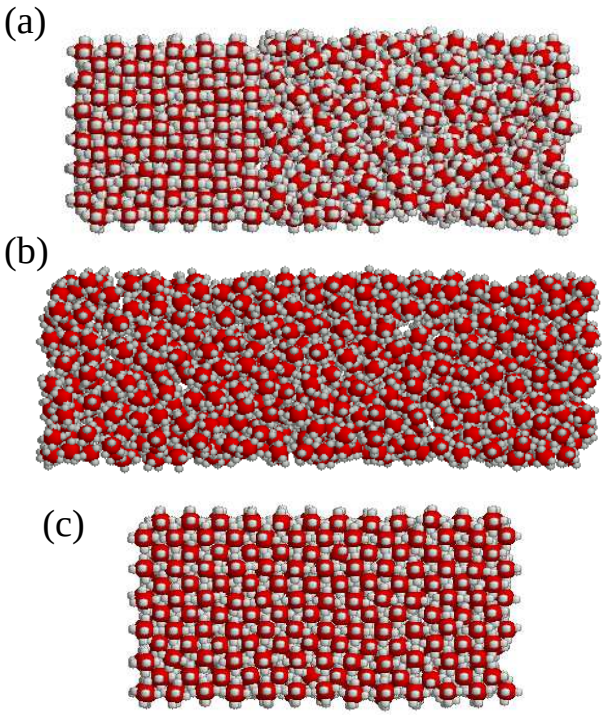

FIG. 5: (Colour online) (a) Snapshot of the initial configuration of the simulation box containing the bcc and the fluid phases in contact. (b) and (c) Snapshots of the final configurations for T^* =0.245 and T^* =0.240, respectively. The pressure was set to p^* =0.1.

For a given pressure, the melting temperature can be estimated performing NpT MC simulations at different temperatures. If the temperature is above the melting point, the solid phase will melt and the energy of the system will increase. On the contrary, if the temperature is below the melting, the solid phase will act as a nucleation seed and the crystal will grow at the expense of the liquid, resulting in a lowering of the system's energy. If it happens that the temperature is equal to the melting temperature, then the solid would be in equilibrium with the liquid, and the energy would remain constant. Using this procedure, we can determine a temperature interval which give upper and lower bounds for the melting temperature.

The results of NpT simulations of a box containing the bcc solid and liquid phases at $p^* = 1.0$ are shown in Figure 4. In this Figure, it can be seen that the melting temperature is approximately $T^*_{melt} = 0.243$. At this temperature the internal energy oscillates around an average value. At temperatures higher than $T^* = 0.243$, the energy increases until it reaches a constant value, that corresponds to the situation when all the solid has melted. Finally, at temperatures lower than $T^* = 0.243$, the energy decreases, again until it reaches a constant value, which, in this case, means that all the fluid has frozen. It is worth noting that both the time for the fluid to freeze and the time for the solid to melt become shorter as the temperature of the system moves further away from the melting temperature. Figure 5 shows the initial configuration of the simulation box, as well as two final states, one above and one below the melting. A visual inspection shows that the final configuration at T^* =0.245 corresponds to an homogeneous fluid phase (Fig. 5 (b)) and, on the contrary, at T^* =0.240 it corresponds to a perfect crystal (Fig. 5 (c)).

III. RESULTS

Let us start by presenting the results for the fluid phase. The free energy of the fluid phase was obtained by thermodynamic integration from the very low density limit, where the fluid can be considered to behave as an ideal gas, to high densities (Equation 5). The integrand of this equation was evaluated by NpT simulations for different densities, and the results were fitted to a polynomial of degree six:

$$\frac{z(\rho^*)-1}{\rho^*} = a_0 + a_1\rho^* + a_2\rho^{*2} + a_3\rho^{*3} + a_4\rho^{*4} + a_5\rho^{*5} + a_6\rho^{*6} \quad (14)$$

The coefficients resulting from this fit for different isotherms are shown in Table I. We have found no evidence of a vapour-liquid transition in any of the isotherms studied, even at the lowest temperature we studied, $T^* = 0.200$. The coefficient a_0 provides an estimation of the second virial coefficient of the model ($B_2 = \lim_{\rho\to 0} \frac{z-1}{\rho}$). As it can be seen, the Boyle temperature, i.e., the temperature for which the second virial coefficient vanishes, is located between 0.200 and 0.243. A more precise estimate can be obtained by determining B_2 from numerical integration. Using this procedure we have computed

T^*	a_0	a_1	a_2	a_3	a_4	a_5	a_6
0.200	-0.6133262	2.3616349	9.5903228	-55.187794	138.527889	-122.51950	-399.33624
0.243	0.1538809	2.6642095	-2.2559535	2.8910917	29.6712406	-39.785495	18.816227
0.500	1.2862246	1.6415799	8.4391218	-30.150196	74.267261	72.615067	28.555569
3.00	1.6574717	2.3183855	-1.5757928	10.982981	-14.129931	10.595277	-2.4231455

TABLE I: Coefficients obtained by fitting the integrand of Equation (5) to a polynomial of degree six (Eq. (14)).

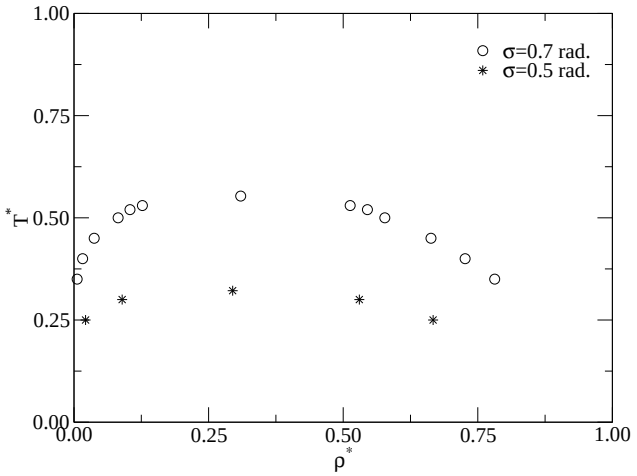

FIG. 6: Dependence of the vapour-liquid coexistence curve on the patch width σ. At lower σ we were unable to find the (metastable) coexistence curves.

B_2 at $T^* = 0.200$, 0.220, 0.230, 0.240, 0.500, obtaining $B_2/\sigma_{LJ}^3 = -0.556, -0.132, 0.031, 0.172, 1.386$. From these results, we estimated that $T^*_{Boyle} \approx 0.228$. An approximation to the critical temperature (T_c) can be obtained from the Boyle temperature. It is known that for another associative model, the primitive model of water, $T_{Boyle}/T_c \approx 1.24$.[4,40] Even though it is not clear how the anisotropy of the model will affect this quotient, we can obtain a rough estimate of the critical temperature. Taking $T^*_{Boyle} \approx 0.228$, $T^*_c \approx 0.18$. This estimate is consistent with the fact that the equation of state of the fluid phase along the isotherm $T^* = 0.200$ does not show any indication of a vapour-liquid equilibrium.

The possibility of a vapour-liquid phase separation was further explored by means of Gibbs ensemble (GE) simulations.[54,55,56] Our GE simulations consisted on 5×10^5 MC cycles for equilibration plus 10^6 MC cycles for obtaining averages, where a MC cycle was defined as N attempts to translate a particle, N attempts to rotate a particle, two attempts to change the volume and about 200 attempts to exchange particles between the two boxes. We simulated a system with 256 particles at a constant total number density $\rho^* = 0.3$. Several patch widths (σ =0.3, 0.5 and 0.7 radians) were considered and we found that, consistent with previous calculations,[7,10] the vapour-liquid coexistence curve is very sensitive to the width of the patches, and that the critical temperature, which was estimated by fitting the GE results to the law of rectilinear diameter and to the critical exponent scaling law,[57,58] decreases as the patches become narrower (see Fig. 6). For the particular case $\sigma = 0.3$ radians, we were unable to locate any vapour-liquid coexistence points, because, in this case, the simulations need to be performed at very low temperatures, where it is particularly difficult to obtain well-converged results. In any case, the observed trends indicate that the critical temperature for $\sigma = 0.3$ must be very low and will fall below the fluid-sc coexistence curve, which is greater than $T^* = 0.2$ up to fairly low densities. These results suggest that if vapour-liquid phase separation does exist, it must be metastable with respect to freezing. This is a relevant finding, because several experimental studies have shown that globular proteins also exhibit a vapour-liquid phase separation that is metastable with respect to solidification.[59,60] Moreover, ten Wolde and Frenkel have suggested that crystallization occurs more rapidly in the proximities of this metastable critical point.[16] In that sense, it would be interesting to determine what is the maximum patch width for which the phase separation between a low density fluid and a high density fluid is metastable.

The free energies of all the solid phases at several thermodynamic states are given in Table II. In some cases, we computed the free energy for two states on the same isotherm, as these can then be used to test the thermodynamic consistency of our results (i.e. the free energy difference between two states as calculated using the Ein-

Structure	T^*	ρ^*	λ^*_{max}	A_{tot}	ΔA_2	ΔA_1	U_0
sc	0.100	0.762	25000	-13.417	-12.644	-29.269	-29.352
bcc	0.100	1.230	20000	-11.637	-10.784	-28.667	-28.723
fcc-o	0.100	1.360	20000	4.355	-11.689	-12.455	-12.508
sc	0.200	0.763	20000	-1.095	-14.284	-14.616	-14.669
bcc	0.200	1.175	20000	0.340	-13.754	-13.719	-13.740
bcc	0.200	1.210	20000	0.690	-13.001	-14.122	-14.146
bcc	0.243	1.147	20000	2.055	-14.754	-11.004	-11.020
fcc-d (PC)	0.500	1.204	20000	5.452	-20.326	-1.971	-1.971
fcc-d (PC)	3.00	1.283	20000	5.488	-21.890	-0.372	-0.373
fcc-d (PC)	3.00	1.376	20000	6.515	-20.941	-0.295	-0.313

TABLE II: Free energy of the solid phases, as obtained by thermodynamic integration from the Einstein crystal. The free energies (A_{tot}, ΔA_2 and ΔA_1) and the lattice energy (U_0) are given in units of Nk_BT.

Solid phase	T^*	b_0	b_1	b_2	b_3	b_4
sc	0.100	26.7846382	-69.2645290	6.67906462	54.0334053	
bcc	0.100	612391.025	-2010382.65	2475295.23	-1354791.73	278126.549
fcc-o	0.100	-631690.341	1383537.04	-1010190.80	245893.687	
bcc	0.243	-570.084541	1657.42401	-1613.44221	525.947816	
fcc-d (PC)	3.00	-1410.40288	3664.08695	-3179.10036	943.459700	

TABLE III: Coefficients of the polynomial fit to the equation of state of the solid phases. The points were fitted to a third-degree polynomial, except for the bcc structure at $T^* = 0.1$, for which a fourth-degree polynomial significantly improves the fit.

stein crystal must be the same as that obtained from integration of the equation of state). In particular, for the bcc phase at $T^* = 0.2$, the difference in free energy between the states at reduced densities 1.210 and 1.175 is $0.350Nk_BT$ as calculated using the Einstein crystal approach, which compares well with the value obtained by integrating the equation of state ($0.355Nk_BT$). For the plastic fcc-d phase at $T^* = 3.0$, the agreement is also good (the free energy difference between the states at reduced densities 1.376 and 1.283 computed using the two methods is 1.027 Nk_BT and 1.034 Nk_BT). This thermodynamic consistency provides positive confirmation of the reliability of the calculations.

The free energy of the solid phases can be obtained at any other point on the isotherm using Eq. 12. The equations of state ($p^*(\rho^*)$) for the solid phases were obtained by performing NpT simulations at different thermodynamic states along a given isotherm and fitting the results of the simulations to a polynomial of the form:

$$p^*(\rho^*) = b_0 + b_1\rho^* + b_2\rho^{*2} + b_3\rho^{*3} + b_4\rho^{*4}. \qquad (15)$$

The resulting data was fitted to a polynomial of degree three, except for the bcc structure at $T^* = 0.1$, for which a fourth-degree polynomial lead to a much better fit. The coefficients resulting from this fitting procedure are shown in Table III.

Using these free energies, we calculated the coexistence points between all the phases that can be at equilibrium, and the results are shown in Table IV. In some cases, we have calculated the coexistence between two phases at two different temperatures, in order to verify that Gibbs-Duhem integration was able to give accurate results even for regions quite far from the starting point.

As a further test of our calculations, the melting points of the solids have also been calculated using the direct coexistence method. The melting points for all the solid phases obtained with this technique are shown in Table V. The agreement between both methods is fairly good, the differences being of the order of 1%.

Using the coexistence points in Table IV as initial conditions, we traced the coexistence curves with the Gibbs-Duhem method. Although we usually integrate the Clapeyron equation, as given by Eq. 13, we sometimes found it more convenient to integrate the equation $dT/dp = (T\Delta v)/(\Delta u + p\Delta v)$. Some of the points obtained with the Gibbs-Duhem are shown in Table VI.

The $T - \rho$ and $p - T$ phase diagrams are shown in Figures 7 and 8, respectively. The dashed line in the diagrams shows a transition between the orientationally-ordered and disordered fcc structures. These points have been estimated by heating the ordered fcc-o structure and monitoring the internal energy. This quantity exhibits a quite abrupt change when orientational order is lost, and the transition temperature was chosen as the temperature where the internal energy curve shows an inflection point.

As expected, the phase diagram shows multiple solid phases. Firstly, at high temperature, where the behaviour is dominated by the repulsions between the particles, the fluid freezes into a plastic crystal phase, the fcc-d phase (i.e., a lattice with fcc structure with respect to the centre of mass, but with orientational disorder). Secondly, at intermediate temperature, it freezes into a

Phase 1	Phase 2	T^*	p^*	ρ_1^*	ρ_2^*	
fluid	fcc-d (PC)	3.00	48.0	1.182	1.270	*
fluid	fcc-d (PC)	0.500	5.55	0.975	1.070	
fluid	bcc	0.243	1.013	0.767	1.107	*
fluid	bcc	0.200	0.339	0.615	1.123	
fluid	sc	0.200	0.048	0.228	0.672	
sc	bcc	0.200	0.709	0.711	1.136	
sc	bcc	0.100	0.444	0.716	1.208	*
bcc	fcc-o	0.100	26.66	1.119	1.407	*

TABLE IV: Coexistence points obtained using the thermodynamic integration method. The points marked with an asterisk were used as the starting points for the Gibbs-Duhem approach. The other points served to test our calculations.

	Direct coexistence		Free energy calculations	
Solid	p^*	T^*	p^*	T^*
sc	0.758	0.232 ± 0.004	0.758	0.229
bcc	1.000	0.243 ± 0.004	1.013	0.243
fcc-d (PC)	48.0	2.97 ± 0.02	48.0	3.00

TABLE V: Melting points obtained using the direct coexistence method. For comparison, the coexistence points obtained from free energy calculations (see table IV) are also shown. Note that the sc-fluid coexistence point was obtained using the Gibbs-Duhem method (see table VI).

Phase 1	Phase 2	p^*	T^*	ρ_1^*	u_1^*	ρ_2^*	u_2^*
fluid	fcc-d (PC)	48.00	2.500	1.149	3.901	1.237	3.198
fluid	fcc-d (PC)	38.19	2.000	1.112	1.913	1.207	1.485
fluid	fcc-d (PC)	12.65	1.000	1.031	0.354	1.126	0.170
fluid	fcc-d (PC)	0.624	0.500	-0.206	-0.482	1.057	-0.303
bcc	fcc-d (PC)	3.42	0.336	1.125	-1.632	1.045	-0.470
bcc	fcc-d (PC)	5.00	0.355	1.156	-1.580	1.121	-0.417
bcc	fcc-d (PC)	7.50	0.363	1.194	-1.648	1.195	-0.353
bcc	fcc-d (PC)	10.25	0.365	1.224	-1.678	1.249	-0.261
bcc	fcc-d (PC)	15.58	0.325	1.265	-1.805	1.322	-0.119
bcc	fcc-d (PC)	22.36	0.250	1.294	-1.949	1.374	-0.048
bcc	fcc-o	26.59	0.040	1.303	-1.648	1.410	-0.353
fluid	bcc	2.915	0.320	0.927	-0.390	1.121	-1.640
fluid	bcc	2.074	0.290	0.873	-0.422	1.113	-1.759
fluid	bcc	0.778	0.230	0.729	-0.494	1.110	-1.964
sc	bcc	0.751	0.225	0.709	-2.154	1.113	-2.004
sc	bcc	0.582	0.150	0.714	-2.493	1.173	-2.381
sc	bcc	0.382	0.080	0.716	-2.746	1.222	-2.677
fluid	sc	0.758	0.229	0.728	-0.494	0.709	-2.133
fluid	sc	0.200	0.218	0.486	-0.378	0.677	-2.165
fluid	sc	0.010	0.181	0.059	-0.070	0.675	-2.333

TABLE VI: Some of the coexistence points obtained with the Gibbs-Duhem method.

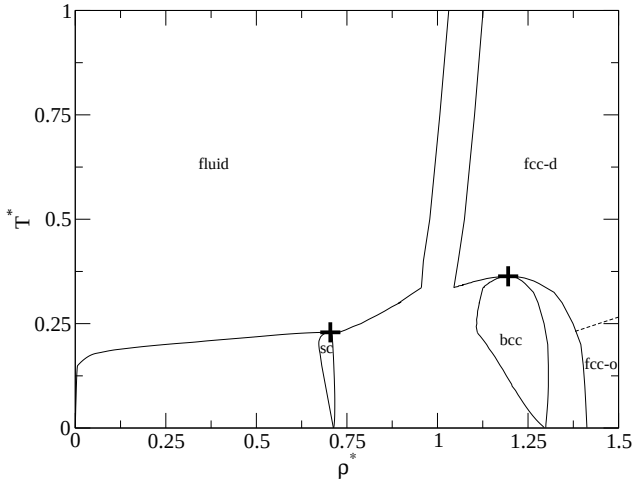

FIG. 7: $T-\rho$ phase diagram of our octahedral six-patch particle system (with σ =0.3). Labels show the region of stability of each phase. The points at which the reentrant behaviour occurs are indicated with a cross.

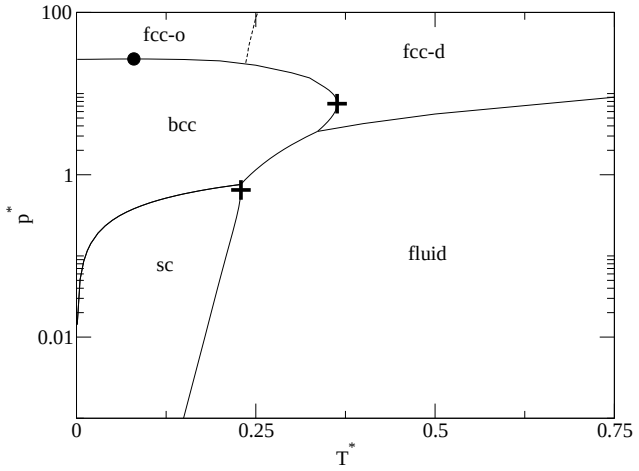

FIG. 8: $p-T$ phase diagram of the octahedral six-patch particle system (with σ =0.3). Labels show the region of stability of each phase. The reentrant behaviour occurs at the points at which there is a change of sign in the slope of the phase boundaries. These points are indicated by a cross. The black circle shows the point where inverse melting occurs.

bcc structure. Finally, at low temperature, it freezes into a low density sc solid. The sc structure is only stable at fairly low pressures, as it is possible to obtain a more dense phase, the bcc crystal, just by introducing a single atom at the centre of the unit cell without a large energetic penalty (see the discussion above and Table II). The bcc phase remains stable up to considerably higher pressures. As the bcc structure is energetically much more favourable than the fcc-o structure (Table II), the bcc crystal is only destabilized at densities for which the first neighbours are at distances close to the LJ repulsive core σ_{LJ}. In the fcc-o structure, the patches are pointing to the second neighbours, which are at a distance considerably larger than the LJ minimum (approximately $\sqrt{2}\sigma_{LJ}$ or larger).

It is worth noting that the sc, bcc and fcc-o phases are all stable at $T^*=0$. At this temperature, the sc and bcc structures are both stable over a finite, but very small range of density, because under these circumstances the solid becomes almost incompressible.

The phase diagram exhibits at least two triple points whose thermodynamic states are given in table VII (we have not studied in detail the triple point where the bcc, fcc-d and fcc-o phases coexist). At one of these triple points, the sc crystal coexists both with the liquid and the bcc solid phases. This triple point is somewhat unusual and a magnified view of this region of the phase diagram is shown in Figure 9. At the triple point, the sc crystal shows a slightly lower density than the liquid, the bcc crystal being the denser phase. The sc crystal is thermodynamically stable in a very narrow window of temperatures above the triple point, and in this region the sc-liquid coexistence lines adopt a dome-like shape. At the top of the dome, the liquid and the sc crystal are in equilibrium, both with the same density. The transition is first order though, because the enthalpy difference between both phases is not zero. For a small range of temperatures below this point, there are two values of the pressure at which the liquid and sc phases are in equilibrium. At the lower coexistence pressure, the sc crystal is the more dense phase. However, the situation is reversed at the higher coexistence pressure, where the liquid is in equilibrium with a lower density sc phase. This means that the coexistence curve shows a reentrant

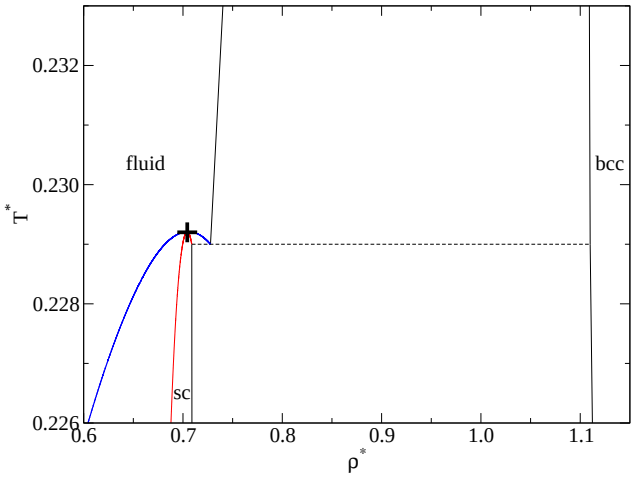

FIG. 9: (Colour online) Detailed view of the phase diagram in the region of the sc-liquid-bcc triple point. The triple point is shown with a dashed line. Labels indicate the region of stability of each phase. The point at which reentrant behaviour occurs is indicated by a cross.

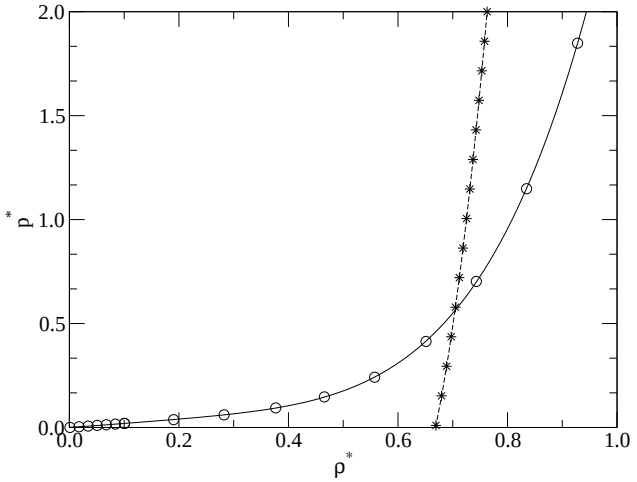

FIG. 10: Equation of state for the liquid phase (circles) and the sc crystal (asterisks) at $T^* = 0.2$.

behaviour in the vicinity of the triple point, i.e. there is a change in the sign of the slope of dp/dT (Fig. 8) at the value of the pressure that coincides with the top of the dome in the $T - \rho$ diagram (Fig. 9). This kind of reentrant behaviour, first speculated by Tammann to occur for water (see Ref.[61]), has been found by computer simulations both for primitive models of water[4] and for realistic models of water.[62] The origin of this behaviour can be seen in Figure 10. Since the compressibility of the solid is very small, the fluid can be less dense and more dense than the solid at different points along an isotherm. This leads to the existence of two coexistence pressures for a given temperature (one low and one high), which results in a reentrant behaviour. The low compressibility

Phase 1	Phase 2	Phase 3	T^*	p^*	ρ_1^*	ρ_2^*	ρ_3^*
sc	liquid	bcc	0.229	0.758	0.709	0.728	1.110
liquid	fcc-d (PC)	bcc	0.336	3.42	0.956	1.045	1.125

TABLE VII: Thermodynamic states for the two triple points in the phase diagram.

of the solid is related to the strong directionality of the patchy bonds in our model (or hydrogen bonds in the case of the water models).

At a higher temperature, there is another triple point, where the fluid, the fcc-d plastic and the bcc crystal are at equilibrium. Curiously, the fcc-d plastic phase can be less dense than the bcc crystal. As the plastic phase is favoured by its high entropy not energy (Table II), the density can change considerably without any accompanying large changes in the energy (as long as the repulsive cores of the particles do not overlap). By contrast, the bcc phase is stabilized by its low energy, and deviations of the second nearest neighbour distance from the minimum in the LJ potential will result in a significant energetic penalty. As a consequence of the wider range of densities possible for the disordered fcc-d phase, the coexistence curves again show a reentrant behaviour and adopt a dome-like shape in the $\rho - T$ phase diagram.

It is also worth mentioning that the bcc–fcc-o coexistence line seems to show inverse melting at very low temperatures ($T^* \approx 0.08$, see black circle in Fig. 8). This inverse melting is different from the reentrant melting mentioned above in the sense that inverse melting is not caused by the fact that both phases have the same density (volume), but because they have the same enthalpy (see Eq. 4). Tammann also speculated about this possibility,[61] and this unusual inverse melting behaviour has previously been observed for ^3He and ^4He and for poly(4-methylpentene-1).[63,64,65]

The results of this work are consistent with previous calculations using a somewhat similar six-patch model,[11] albeit with differences due to the differences in the potentials used. Chang *et al.* also found several solid phases, including the plastic fcc-d phase at high temperatures, an ordered fcc solid at moderate pressures and low temperatures, and a sc solid at low temperatures and pressures.[11]

IV. CONCLUSIONS

We have computed the phase diagram of particles with six octahedrally-arranged patches for a case where the patches are relatively narrow. Even for this relatively simple potential, a complex phase diagram results with competition between multiple solid phases differing both in their density and whether they are orientationally ordered, and with unusual features such as reentrance and inverse melting.

Consistent with previous results,[7,10,11] there is no stable gas-liquid phase separation in our model. The lowest-

energy structure is a simple cubic crystal, but this structure is only stable at relatively low pressure. As the pressure increases, first a bcc and then an fcc phase become most stable, where both phases are orientationally ordered. However, on increasing the temperature, entropic effects become more important and a plastic fcc crystal becomes most stable.

Even though we have considered very simple anisotropic models, they are able to predict the formation of low density crystals, in analogy with the preference of the proteins to form open crystals. In that sense, even though our model is still far from real proteins, our work can potentially provide some insights into the complex fluid-solid equilibrium of proteins. In future work, it will be interesting to explore how the geometry and number of the patches will influence the phase diagram, and in particular the structure of the stable crystalline phases. Particularly relevant to proteins may be the exploration of random, rather than just ordered, arrangements of the patches.

Although our calculations have determined the region of thermodynamic stability for each phase, it does not necessarily follow that these phases will be easily accessible from within these regions. Indeed there is increasing evidence that the dynamics of crystal nucleation can depend sensitively on the nature of the crystalline phase and also of the liquid,[66,67,68,69] as has been seen in preliminary calculations for the current model.[32] Therefore, in future work we are planning to study the nucleation dynamics for the current model, and in particular to explore how this dynamics depends on the geometry of the patches. Such information might provide important insights that could help colloidal chemists in designing their anisotropic particles to crystallize into the desired target structure.

Acknowledgments

This work was funded by grants FIS2004-06227-C02-02 of Dirección General de Investigación and S-0505/ESP/0229 of Comunidad Autónoma de Madrid. We would also like to acknowledge financial help from projects MTKD-CT-2004-509249 from the European Union and from project 910570 from the Universidad Computense de Madrid. E.G.N. wishes to thank the Ministerio de Educación y Ciencia and the Universidad Complutense de Madrid for a Juan de la Cierva fellowship, and J.P.K.D. and A.A.L. are grateful to the Royal Society for financial support. We would like to thank David J. Wales and Mark A. Miller for useful discussions, and Emanuela Zaccarelli and Francesco Sciortino for organizing the interesting workshop entitled: *Patchy Colloids, Proteins and Network Forming Liquids: Analogies and new insights from computer simulations*, held at the CECAM. We are also grateful to F. Sciortino for sending us a copy of Reference 40 prior to publication.

[1] J. Kolafa and I. Nezbeda, Mol. Phys. **61**, 161 (1987).
[2] G. Jackson, W. G. Chapman, and K. E. Gubbins, Mol. Phys. **65**, 1 (1988).
[3] R. Sear and G. Jackson, J. Chem. Phys. **105**, 1113 (1996).
[4] C. Vega and P. A. Monson, J. Chem. Phys. **109**, 9938 (1998).
[5] M. N. Garcia-Lisbona, A. Galindo, G. Jackson, and A. N. Burgess, Mol. Phys. **93**, 57 (1998).
[6] M. H. Ford, S. M. Auerbach, and P. A. Monson, J. Chem. Phys. **121**, 8415 (2004).
[7] R. P. Sear, J. Chem. Phys. **111**, 4800 (1999).
[8] X. Song, Phys. Rev. E **66**, 011909 (2002).
[9] N. M. Dixit and C. F. Zukoski, J. Chem. Phys. **117**, 8540 (2002).
[10] N. Kern and D. Frenkel, J. Chem. Phys. **118**, 9882 (2003).
[11] J. Chang, A. M. Lenhoff, and S. I. Sandler, J. Chem. Phys. **120**, 3003 (2004).
[12] J. Chang, A. M. Lenhoff, and S. I. Sandler, J. Phys. Chem. B **109**, 19507 (2005).
[13] V. Talanquer, J. Chem. Phys. **120**, 084704 (2004).
[14] P. G. Vekilov and A. A. Chernov, Solid State Physics **57**, 1 (2002).
[15] D. Rosenbaum, P. C. Zamora, and C. F. Zukoski, Phys. Rev. Lett. **21**, 1407 (1996).
[16] P. R. ten Wolde and D. Frenkel, Science **277**, 1975 (1997).
[17] B. W. Matthews, J. Mol. Biol. **33**, 491 (1968).
[18] H. R. Sheu, M. S. El-Aasser, and J. W. Vanderhoff, J. Polym. Sci. A **28**, 629 (1990).
[19] V. N. Manoharan, M. T. Elsesser, and D. J. Pine, Science **301**, 483 (2003).
[20] Y.-S. Cho, G.-R. Yi, J.-M. Li, S.-H. Kim, V. M. Manoharan, D. J. Pine, and S. M. Yang, J. Am. Chem. Soc. **127**, 15968 (2005).
[21] Y.-S. Cho, G.-R. Yi, S.-H. Kim, D. J. Pine, and S. M. Yang, Chem. Mat. **17**, 5006 (2005).
[22] K.-H. Roh, D. C. Martin, and J. Lahann, Nature Materials **4**, 759 (2005).
[23] C. E. Snyder, A. M. Yake, J. D. Feick, and D. Velegol, Langmuir **21**, 4813 (2005).
[24] Z. F. Li, D. Y. Lee, M. F. Rubner, and R. E. Cohen, Macromolecules **38**, 7876 (2005).
[25] A. van Blaaderen, Science **439**, 545 (2006).
[26] K.-H. Roh, D. C. Martin, and J. Lahann, J. Am. Chem. Soc. **128**, 6796 (2006).
[27] A. M. Jackson, J. W. Myerson, and F. Stellacci, Nature Materials **3**, 330 (2004).
[28] R. Lévy, ChemBioChem **7**, 1141 (2006).
[29] G. A. DeVries, M. Brunnbauer, Y. Hu, A. M. Jackson, B. Long, B. T. Neltner, O. Uzun, B. H. Wunsch, and F. Stellacci, Science **315**, 358 (2007).
[30] A.-P. Hynninen, J. H. J. Thijssen, E. C. M. Vermolen, M. Dijkstra, and A. van Blaaderen, Nature Materials **6**, 202 (2007).
[31] Z. Zhang, A. S. Keys, T. Chen, and S. C. Glotzer, Langmuir **21**, 11547 (2005).
[32] J. P. K. Doye, A. A. Louis, I.-C. Lin, L. R. Allen, E. G.

Noya, A. W. Wilber, H. C. Kok, and R. Lyus, Phys. Chem. Chem. Phys. **9**, 2197 (2007).
[33] Z. Zhang and S. C. Glotzer, Nano Letters **21**, 1407 (2004).
[34] M. F. Hagan and D. Chandler, Biophys. J. **91**, 42 (2006).
[35] K. V. Workum and J. F. Douglas, Phys. Rev. E **73**, 031502 (2006).
[36] A. W. Wilber, J. P. K. Doye, A. A. Louis, E. G. Noya, M. A. Miller, and P. Wong, arXiv.org (cond-mat/0606634) (2007).
[37] C. D. Michelle, S. Grabielli, P. Tartaglia, and F. Sciortino, J. Phys. Chem. B **110**, 8064 (2006).
[38] E. Bianchi, J. Largo, P. Tartaglia, E. Zaccarelli, and F. Sciortino, Phys. Rev. Lett. **97**, 168301 (2006).
[39] F. Sciortino, E. Bianchi, J. F. Douglas, and P. Tartaglia, arXiv.org:cond-mat/0701531 (2007).
[40] F. Romano, P. Tartaglia, and F. Sciortino, arXiv.org (cond-mat/0703372) (2007).
[41] V. F. Petrenko and R. W. Whitworth, *Physics of Ice* (Oxford University Press, Oxford, 1999).
[42] A.-P. Hynninen, M. E. Leunissen, A. van Blaaderen, and M. Dijkstra, Phys. Rev. Lett. **96**, 018303 (2006).
[43] D. Frenkel and A. J. C. Ladd, J. Chem. Phys. **81**, 3188 (1984).
[44] D. Frenkel and B. Smit, *Understanding Molecular Simulation. From Algorithms to Applications* (Academic Press, Boston, 1996).
[45] D. Frenkel and B. M. Mulder, Mol. Phys. **55**, 1171 (1985).
[46] C. Vega, E. P. A. Paras, and P. A. Monson, J. Chem. Phys. **96**, 9060 (1992).
[47] C. Vega, E. P. A. Paras, and P. A. Monson, J. Chem. Phys. **97**, 8543 (1992).
[48] J. W. Schroer and P. A. Monson, J. Chem. Phys. **112**, 8950 (2000).
[49] C. Vega and P. A. Monson, J. Chem. Phys. **102**, 1361 (1995).
[50] D. A. Kofke, J. Chem. Phys. **98**, 4149 (1993).
[51] D. A. Kofke, Mol. Phys. **78**, 1331 (1993).
[52] A. Ladd and L. Woodcock, Chem. Phys. Lett. **51**, 155 (1977).
[53] R. G. Fernández, J. L. Abascal, and C. Vega, J. Chem. Phys. **124**, 144506 (2006).
[54] A. Z. Panagiotopoulos, Mol. Phys. **61**, 813 (1987).
[55] A. Z. Panagiotopoulos, N. Quirke, M. Stapleton, and D. Tildesley, Mol. Phys. **63**, 527 (1988).
[56] B. Smit, P. de Smedt, and D. Frenkel, Mol. Phys. **68**, 931 (1989).
[57] E. A. Guggenheim, J. Chem. Phys. **13**, 253 (1945).
[58] J. S. Rowlinson and F. L. Swinton, *Liquids and Liquid Mixtures* (Butterworths, London, 1982).
[59] M. L. Broide, C. R. Berland, J. Pande, O. Ogun, and G. B. Benedek, Proc. Natl. Acad. Sci. USA **88**, 5660 (1991).
[60] M. Muschol and F. Rosenberger, J. Chem. Phys. **107**, 1953 (1997).
[61] P. W. Bridgman, Proc. Am. Acad. Arts Sci. **47**, 441 (1912).
[62] E. Sanz, C. Vega, J. L. F. Abascal, and L. G. MacDowell, Phys. Rev. Lett. **92**, 255701 (2004).
[63] S. Rastogi, G. W. H. Höhnre, and A. Keller, Macromolecules **32**, 8897 (1999).
[64] A. L. Greer, Nature **404**, 134 (2000).
[65] F. H. Stillinger and P. G. Debenedetti, Biophys. Chem. **105**, 211 (2003).
[66] J. R. Fernández and P. Harrowell, Phys. Rev. E **67**, 011403 (2003).
[67] K. F. Kelton, A. L. Greer, H. D. M., and D. Holland-Moritz, MRS. Bull. **29**, 940 (2004).
[68] V. Molinero, S. Sastry, and C. A. Angell, Phys. Rev. Lett. **97**, 075701 (2006).
[69] R. P. Sear, J. Phys.: Condens. Matter **19**, 033101 (2007).